# APPLICATION OF LATTICE-BOLTZMANN METHOD TO ROTORCRAFT AERODYNAMICS AND AEROACOUSTICS

Gianluca Romani and Damiano Casalino

Aerodynamics, Wind Energy, Flight Performance and Propulsion Department, Delft University of Technology, Delft, The Netherlands

**Abstract**

The aim of this work is to evaluate the accuracy and the computational performances of the CFD/CAA solver PowerFLOW®, developed and distributed by Exa Corporation, to predict the unsteady aerodynamic loads, the rotor wake development and the noise radiation of helicopters in Blade-Vortex Interaction conditions. The employed benchmark configuration is the 40% geometrically and aeroelastically scaled model of a BO-105 4-bladed main rotor tested in the open-jet anechoic test section of the German-Dutch wind tunnel in the framework of the HART-II project. In the present study, only the baseline operating condition of the test matrix, without higher harmonic control, is considered. All simulations are performed by assuming a rigid blade motion, but a computational strategy is employed to take into account the effective elastic deformation motion of the blade measured during the experiments. As expected, modeling the elastic blade motion leads to more accurate predictions of both unsteady air-loads and noise footprint. The effects of the mesh resolution on the aerodynamic and aeroacoustic prediction is investigated. As a conclusive effort, the effects of fuselage scattering on the noise footprint are evaluated by using the same computational model to simulate two additional configurations: the isolated rotor of the HART-II configuration and the same rotor installed on a different helicopter fuselage. Significant far-field noise scattering effects are observed.

## 1. INTRODUCTION

This work describes an application of the Lattice-Boltzmann Method (LBM) software PowerFLOW® to the evaluation of the aerodynamic and aeroacoustic fields around helicopter rotors in strong Blade-Vortex Interaction (BVI) conditions.

Helicopter BVI is a phenomenon which occurs when a rotor blade interacts very closely with tip vortices released by the other blades, and it typically occurs during descent flights or maneuvers at moderate advance ratio, when the wake of the main rotor remains very close to the rotor itself. The induced fluctuations of the blade aerodynamic loads represent one of the main sources of helicopter community noise and fuselage vibration. BVI noise is indeed considered one of the major limitations of helicopter operation in urban areas, and it is strongly correlated with hundreds of dormant heliports worldwide.

Due to the impulsive character of BVI, the radiated noise spectrum is rich of harmonics in the mid-frequency range, with wavelengths that can be smaller than the characteristic dimension of the helicopter fuselage. As a consequence, the acoustic field around the helicopter is potentially affected by the presence of the fuselage and the surrounding perturbed flow, a phenomenon which is referred to as fuselage scattering, say the combination of reflection, diffraction and flow-induced refraction effects.

The physics of BVI is governed by the structure and trajectory of the tip vortices, and in particular by the minimum distance from the rotor blade, which is referred to as blade-vortex miss distance[1]. For this reason, in order to successfully predict BVI phenomena, it is required to adopt an aerodynamic solver able to accurately predict three-dimensional unsteady flows and the spatial evolution of the wake vorticity, as well as to take into account the periodic elastic deformation of the rotor blades.

In the last two decades, many researchers have focused their efforts on experimental characterization and numerical prediction of BVI. In this framework, the second Higher-Harmonic Control (HHC) Aeroacoustic Rotor Test (HART-II) represents the best-known benchmark case for helicopter aerodynamics, aeroelasticity and aeroacoustics[2,3,4,5,6,7]. The HART-II experiments were conducted in the large low-speed facility of the German-Dutch wind tunnel (DNW) in 2001 by an international cooperation between DLR, Onera, DNW, US Army AFDD and NASA Langley. The HART-II experimental database includes blade deflections, section air-loads, wake geometry, PIV and acoustic radiation measurements. Due to the large and comprehensive data sets available, the HART-II database is widely used by the rotorcraft research community for the validation of numerical solvers. In Refs.[8,9] an assessment of the state-of-the-art of the comprehensive codes used within the HART II International Workshop is provided, whereas in Refs.[10,11] a review of the state-of-the-art of Computational Fluid Dynamics methods coupled with Computational Structural Dynamics codes (CFD/CSD) is presented. Comprehensive codes are typically based on finite element beam formulations as structural model and two-dimensional blade-section theories, enhanced by corrections for unsteadiness and free-wake vortex lattice approaches to include the rotor wake influence on the aerodynamic loads. The main advantage of comprehensive codes is the significantly lower CPU cost compared to CFD/CSD coupled approaches. Nevertheless, comprehensive codes typically requires to tune some of the parameters involved in their aerodynamic modules to obtain a good agreement between experimental data and numerical results, and they offer a quite lower potential in terms of accuracy and access to flow physical quantities with respect to that provided by CFD-based methods. For both the aforementioned approaches, the noise radiation is typically evaluated using formulations based on the Ffowcs-Williams & Hawkings (FW-H) acoustic analogy equation[12] applied to the rotor aerodynamic solution.

The main goal of this paper is to simulate the HART-II baseline configuration, without HHC, using the recently released version 5.4 of the LBM-based solver PowerFLOW®. More precisely, a newly released LBM formulation is employed, which extends the applicability of the LBM formulation to transonic flow conditions[13]. It is worth mentioning that the use of LBM to accomplish a rotorcraft aerodynamic and aeroacoustic benchmark study constitutes an original contribution of the present work. The benchmark study is conducted by investigating the effects of mesh resolution first, and then by analyzing the impact of different blade deformation modeling assumptions on the accuracy of the aerodynamic and acoustic results. The performances of the solver are reported for the sake of comparison with those of conventional CFD methods based on the discretization of Unsteady Reynolds Average Navier-Stokes (URANS) equations, which are supposed to generate an equivalent amount of flow information at an equivalent level of fidelity. Finally, the fuselage scattering effects are investigated by comparing the noise footprint with/without fuselage and with a different fuselage geometry. This kind of analysis, based on a compressible unsteady flow simulation and a direct application of the FW-H analogy, constitutes a further element of originality of the present work.

The paper is organized as follows. In Section 2, an overview of the underlying elements of the LBM-Very Large Eddy Simulation (VLES) are presented, along with the computational strategy adopted to take into account the effects due to the elastic motion of the blades. Section 3 is focused on the effects of the mesh resolution and blade deformation on the accuracy of the numerical predictions. In Section 4 the fuselage scattering effects are analyzed by comparing different sets of computational results. Finally, the main conclusions of this work are drawn in the conclusive section.

## 2. NUMERICAL APPROACH

In this section, the underlying elements of the LBM-VLES model implemented in PowerFLOW® are presented first. Then, a description of the computational approach adopted to model the experimental blade elastic deformation is provided.

### 2.1. LBM-VLES flow model

The LBM core of the PowerFLOW® CFD/CAA software solves the Boltzmann equation for the distribution function $f(\mathbf{x}, t, \mathbf{v})$ on a hexahedral mesh automatically generated around bodies, which consist of one or more connected solid parts. The function $f$ represents the probability to find, in the elementary volume $d\mathbf{x}$ around $\mathbf{x}$ and in the infinitesimal time interval $(t, t + dt)$, a number of fluid particles with velocity in the interval $(\mathbf{v}, \mathbf{v} + d\mathbf{v})$. The Boltzmann equation is solved by discretizing the space velocity domain into a prescribed number of values in magnitude and direction. These discrete velocity vectors are such that, in a prescribed time step, one particle can be advected from one point of the mesh to $N$ neighboring points, including the point itself. For transonic flow simulations[13], a number of $39$ stencil points are used (D3Q39, say $3$ dimensions, $39$ velocity states). It can be demonstrated that using $39$ particle velocity states ensures sufficient lattice symmetry to recover the Navier-Stokes equations for a non isothermal flow up to a Mach number of about $2$[14]. The standard LBM formulation is based on the time-explicit advection equation $f_i(\mathbf{x} + \mathbf{v}_i \Delta t, t + \Delta t) - f_i(\mathbf{v}, t) = C_i(\mathbf{v}, t)$. The collision term $C_i$ is modeled with the well-known Bhatnagar-Gross-Krook (BGK) approximation[14,15], i.e. $C_i(\mathbf{x}, t) = \Delta t/\tau[f_i(\mathbf{x}, t) - f_i^{eq}(\mathbf{x}, t)]$, where $\tau$ is the relaxation time, which is related to the fluid viscosity and temperature, and $f_i^{eq}$ is the equilibrium distribution function, which is approximated by a fifth-order expansion with constant temperature[14]. Once the distribution function is computed, flow density and linear momentum can be determined through discrete integration, i.e. $\rho(\mathbf{x}, t) = \sum_i f_i(\mathbf{x}, t)$ and $\rho\mathbf{u}(\mathbf{x}, t) = \sum_i f_i(\mathbf{x}, t)\mathbf{v}_i$. All the other physical quantities can be determined through thermodynamic relationships for an ideal gas.

Solving the lattice Boltzmann equation is equivalent to performing a Direct Numerical Simulation (DNS) of the Navier-Stokes equations in the limits of the dynamic range (Mach number) that can be accurately covered by the number of discrete particle velocity vectors, and in the limits of the lattice resolution required to capture the smallest scales of turbulence. For high Reynolds flows, turbulence modeling is introduced[16] into the LBM scheme by solving a variant of the renormalization group (RNG) $k-\epsilon$ model[17,18] on the unresolved scales[19], selected via a swirl model[20]. This approach is referred to as LBM Very Large Eddy Simulation (LBM-VLES).

Because resolving the wall boundary layer by using a Cartesian mesh approach down to the viscous sublayer in high Reynolds number applications is prohibitively expensive, a wall function approach is used in PowerFLOW® to model boundary layers on solid surfaces. The wall function model is an extension of the standard formulation, but it includes the effects of favorable and adverse pressure gradients, and accounts for surface roughness through a length parameter.[21].

The LBM scheme is solved on a grid composed of cubic volumetric elements (voxels), the lattice, which is automatically created by the code. A Variable Resolution (VR) by a factor of two is allowed between adjacent regions. Consistently, the time step is varied by a factor two between adjacent resolution regions. Solid surfaces are automatically facetized within each voxel intersecting the wall geometry using planar surface elements (surfels). For the no-slip and slip wall boundary conditions at each of these elements, a boundary scheme[22] is implemented, based on a particle bounce-back process and a specular reflection process, respectively. Therefore, very complex arbitrary geometries can be treated automatically by the LBM solver.

The local character of the LBM scheme allows an efficient parallelization of the solver. Due to the fact that the LBM is low dissipative, compressible and provides an unsteady solution, it is intrinsically suited for aeroacoustic simulations. Indeed, the usage of PowerFLOW to accurately tackle unsteady flow problems of industrial relevance is quite an established practice in the field of fixed-wing aircraft aeroacoustics, both at component level[23,24] and full aircraft level[25,26]. More recently, the solver has been also used by Casalino *et al*[27] to predict the broadband noise generated by the $22$-in Source Diagnostic Test (SDT) fan rig of the NASA Glenn Research Center[28] with an accuracy in the order of the experimental uncertainty of $1$ dB.

The necessity to accurately capture the near-field noise propagation from the source region up to the FW-H integration surface is a requirement that can take advantage of the intrinsic low-dissipation and low-dispersion properties of the LBM scheme compared to partial differential equation discretization schemes. The CAA properties of LBM allows to analyze the acoustic near-field directly extracted from the transient flow solution. In this work, both direct noise computations and FW-H far-field computations are performed. The employed FW-H approach is based on a forward-time solution[29] of Farassat's formulation 1A[30] extended to a permeable integration surface[31]. The FW-H code is part of Exa's post-processing software PowerACOUSTICS® 4.1, which is also used to perform statistical and spectral analysis of any unsteady solution generated by PowerFLOW® (volume/surface fields and probe signals).

### 2.2. Blade deformation model

The main affecting parameter of BVI phenomenon is the blade-vortex miss distance, which results from the instantaneous position of the convected tip vortices and the deformable blades. On one hand, the accurate prediction of the vortex trajectory relies on the capability of the aerodynamic solver to convect vorticity with low dissipation and dispersion, thus preserving the vortex coherence over a sufficient number of rotor revolutions. On the other hand, the accurate prediction of the instantaneous position of different blade sections relies on the capability to model the elastic deformation of the blade under non-inertial and aerodynamic loads. Therefore two-way-coupled high-fidelity CFD/CSD models are the ultimate frontier of predictive BVI noise. As a primary step along methodology maturation path, the present work is focused on the aerodynamic model only, and the flapping and torsional deformations are prescribed as measured in the HART-II experiments by means of Stereoscopic Pattern Recognition (SPR) technique[32,33,34]. More precisely, since the measurements were conducted using a coarse resolution, both in the azimuthal and radial directions, and since several measurement points were missing, an analytical reconstructions of the elastic blade motion is used in this work, which was performed by projecting Fourier components of the measured deformation on a basis of low-order FEM-computed modal shapes. Following van der Wall[35], the flap, lead-lag and torsion deformations for each blade can be respectively written as:

$$(1)\quad z(r,\Psi) = \sum_{i=1}^{3} q_{z_i}(\Psi)\phi_{z_i}(r)$$

$$(2)\quad y(r,\Psi) = \sum_{i=1}^{2} q_{y_i}(\Psi)\phi_{y_i}(r)$$

$$(3)\quad \phi(r,\Psi) = \sum_{i=1}^{2} q_{x_i}(\Psi)\phi_{x_i}(r),$$

where $\phi_{z_i}$, $\phi_{y_i}$ and $\phi_{x_i}$ are the modal shapes, functions of the radial coordinate $r$, and $q_{z_i}$, $q_{y_i}$ and $q_{x_i}$ are the generalized coordinates which reproduce the periodic time dependency of each elastic deformation component through the azimuthal angle $\Psi = \Omega t$, with $\Omega$ denoting the rotational speed of the rotor.

In this work, the blade elastic deformation is modeled by prescribing a combination of rigid motion and transpiration velocity boundary condition on the surface of the blades. This approach follows from the idea that a small-amplitude motion of the blade around its mean position can be modeled by applying a velocity wall boundary condition that has an equivalent dynamic effect on the blade. This approximation is imposed by the main limitation of the solver, which can simulate a combination of rigid rotations, but not a time-dependent deformation of the geometry. The computational mesh is in fact generated automatically by the solver in a pre-processing stage and it is used throughout the simulation. The rigid rotation of parts respect to others is managed by creating partitions of the volume mesh in relative rotation. More specifically, in this work, the blade flapping deformation is modeled by prescribing a wall velocity boundary condition equal to the time-derivative of Eq.(1) along the direction normal to the blade chord. The torsional deformation, instead, is modeled by prescribing a combination of a rigid blade pitching motion, equal to the experimental torsion at the $70\%$ of the blade span, and a wall velocity boundary condition for the residual torsional component, namely the total torsion minus the one at the $70\%$ of blade span. The first torsional contribution, say:

$$\text{(4)} \quad \phi(r = 0.7R, \Psi) = \sum_{i=1}^{2} q_{x_i}(\Psi)\phi_{x_i}(r = 0.7R),$$

is added to the rigid blade pithing command, whereas the second contribution is modeled by prescribing the residual part of the torsion $\Delta\phi(r, \Psi) = \phi(r, \Psi) - \phi(r = 0.7R, \Psi)$ as a dynamically equivalent flapping motion $\dot{z}^{eq}(r, \Psi)$ along the direction normal to the blade chord, say:

$$\text{(5)} \quad \dot{z}^{eq}(r, \Psi) = -kU(r, \Psi)\tan(\Delta\phi(r, \Psi)),$$

where $k$ is a tuning parameter, and $U(r, \Psi) = \Omega r + U_\infty \sin(\Psi)$ is the local blade section velocity. Finally, the lead-lag deflection motion is not expected to affect the BVI phenomenon significantly and is therefore neglected in the present study.

## 3. NUMERICAL RESULTS

In this section, a mesh resolution study is firstly conducted in order to establish a confidence level for the employed numerical setup. Then, the effects due to the incorporation of the blade elastic deformation in the numerical setup are investigated. The numerical results are compared to the experimental data from the HART-II test.

All simulations performed in this work are based on the same rotor operating conditions, which is the HART-II baseline configuration without HHC, corresponding to a descent flight in strong BVI conditions. The rotor shaft angle is $\alpha_s = 4.5°$, the rotational speed of the rotor is $\Omega = 109.12$ rad/sec, and the advance ratio is $\mu = 0.15$. The same experimental collective and cyclic blade pitch commands are used for all simulations, say $\theta_0 = 3.8°$, $\theta_c = 1.92°$ and $\theta_s = -1.34°$ respectively. A spherical simulation volume of radius $100R$ centered around the helicopter is used. The rotor radius is $R = 2$ m. Static pressure and the freestream velocity are proscribed on the outer boundary, and an acoustic sponge approach is used to damp the out-going acoustic waves and thus minimize the backward reflection from the outer boundary. Figures 1(a) and 1(b) show the computational grid used for all simulations presented in this section. The finest VR level is set around the blades. The second finest VR is used to fill a blade tip annuls and cylinders encompassing the blades, which are also used to define the blade pitching volumes.

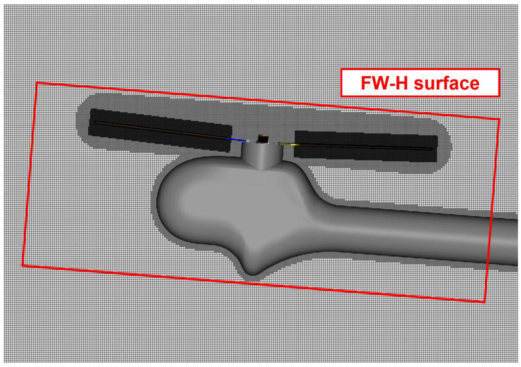


(a) *Side view*

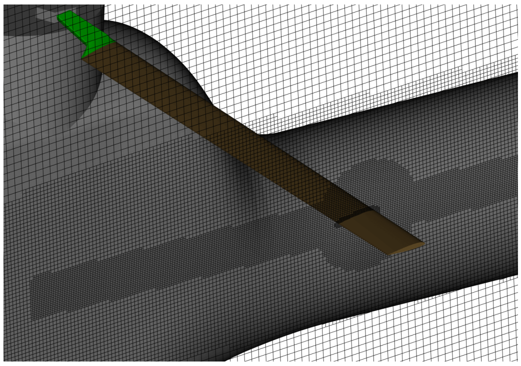

(b) *Close-up view*

Figure 1: Computational grid around the helicopter model, every second line shown for visualization purposes.

Throughout this paper, the noise radiation is computed both by extracting the pressure signals directly from the CFD solution and by using a FW-H acoustic analogy applied to a permeable surface encompassing the whole helicopter model, as sketched in Fig. 1. Acoustic data are sampled at $68$ kHz along $2$ rotor revolutions ($0.115\,\mathrm{sec}$), after a settling time of $4$ rotor revolutions ($0.23\,\mathrm{sec}$). Fourier transforms of the near-field pressure are evaluated using a bandwidth of $35.3$ Hz, $20\%$ window overlap coefficient and Hanning weighting.

### 3.1. Mesh resolution effects

As a sanity check of the quality of the computational mesh, a preliminary grid convergence study is conducted by taking into account the elastic deformation of the blade, as discussed in Section 2.2. Three resolution levels are considered, hereinafter referred as *coarse*, *medium* and *fine*, corresponding to $N = 42$, $60$ and $85$ voxels per blade chord ($c = 0.121\,\mathrm{m}$) in the finest VR, respectively ($\sqrt{2}$ refinement ratio). The whole computational mesh is refined accordingly using the same VR scheme for all simulations. A summary of the grid size and the computational cost for the three refinement cases is reported in Table 1. Simulations are performed using $720$ cores Intel Sandybridge $2.7$ GHz and require, for the finest case, $3.6$ hours per rotor revolution.

| Res. level | N | # Voxels | # Surfels | CPUh/rev |
|---|---|---|---|---|
| Coarse | 42 | 89 | 5.4 | 696 |
| Medium | 60 | 167 | 6.7 | 1203 |
| Fine | 85 | 406 | 11.9 | 2598 |

Table 1: Grid size in million of elements and computational cost.

The mesh convergence is first examined in terms of trend of the Mean-Squared Relative Error (MSRE) between rotor thrust time-histories of two consecutive resolution levels. Considering the steady statistically converged rotor thrust, the MSRE resulted in $0.0018$ and $0.0013$ for coarse-medium and medium-fine cases, respectively, thus revealing a convergence trend.

Figures 2(a) to 2(c) show instantaneous snapshots of the blade tip-vortex system for the three resolution levels extracted according to the $\lambda_2$ criterion. These images qualitatively illustrate that higher mesh resolutions result in lower diffusion of the vortical structures, which preserve their coherent character over a larger number of spirals. This aspect is crucial for an accurate BVI noise prediction generated by the interaction between one blade and the series of vortices from all blades. Interestingly, a multitude of turbulent scales can be observed, in particular in the advancing side of the rotor, where vortex breakdown occurs because of the higher relative velocities and strain rates. This is one of the advantages of a VLES turbulence modeling compared to URANS, and it is crucial to predict broadband noise components.

The sensitivity of the aerodynamic solution to the grid resolution is now evaluated in terms of unsteady

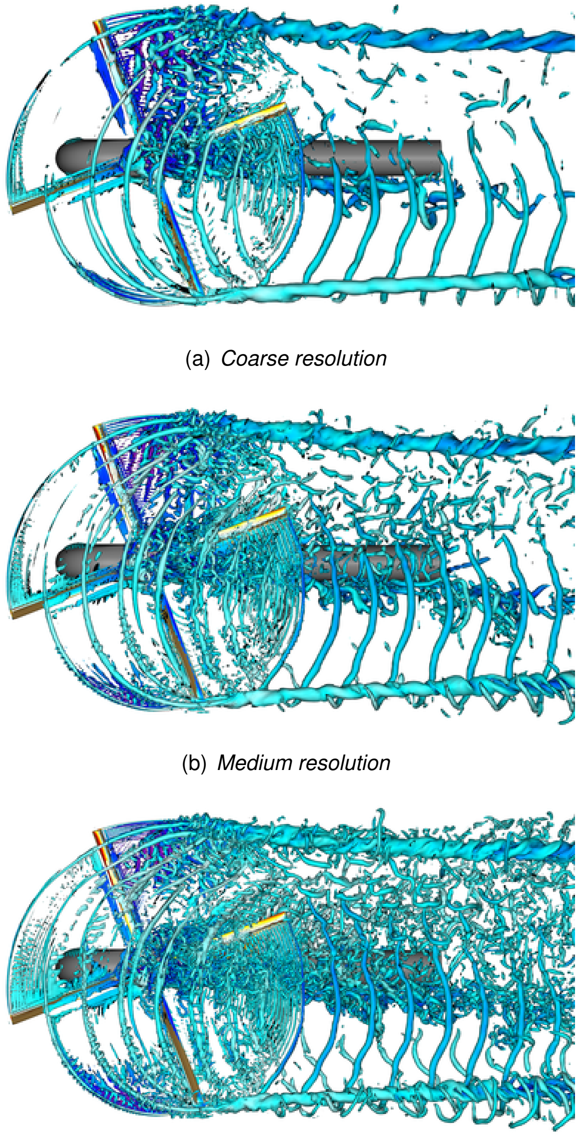

(a) *Coarse resolution*

(b) *Medium resolution*

(c) *Fine resolution*

Figure 2: $\lambda_2 = -5000\ 1/s^2$ iso-surfaces of the instantaneous flow around the main rotor colored by velocity magnitude.

air-loads, i.e. $c_n M^2$, where $c_n$ is the section normal force coefficient and $M$ is the local Mach number. For each resolution level, Figure 3(a) shows the low-frequency content time history (up to the $10$/rev harmonic) of $c_n M^2$ coefficient at the span-wise section located at $r/R = 0.87$, while Figure 3(b) depicts the high-frequency $c_n M^2$ time history (above the $10$/rev harmonic) at the same blade span-wise position. It is worth mentioning that the low-frequency $c_n M^2$ is mainly influenced by the rigid and elastic motion of the blade and thus gives a good indication on the quality of the employed elastic deformation model, whereas the high-frequency $c_n M^2$ is mostly affected by BVI and hence can be used to examine the adequacy of the computational setup to predict BVI noise.

The low-frequency $c_n M^2$ content exhibits a certain grid dependence, but a convergence trend can be observed. The highest differences between the three numerical data sets take place between $90°$ and $270°$ in the azimuth. These are probably due to the slightly different resolved up-wash velocity field induced by the front part of the helicopter fuselage, and to the different resolution of the discrete blades on which the velocity boundary condition is applied. The largest discrepancies between measurements and predictions take place in the downstream semi-disk.

More interestingly, the high-frequency $c_n M^2$, which is directly connected with the BVI phenomenon, shows a clearer convergence trend, and the amplitude of the load fluctuations induced by the vortices are better captured when the fine mesh resolution is used, especially in the advancing side where, among others, the spurious fluctuations around $85°$ tend to disappear as the mesh resolution is increased. Conversely, the fluctuations in the retreating side seem to be less affected by the mesh resolution.

The mesh resolution analysis is concluded by examining the sensitivity of the noise radiation to the grid refinement. To this purpose, Figure 4 shows the comparison between the experimental noise footprint on a horizontal plane located $2.2$ m below the rotor hub and the numerical ones. Here, the noise contour maps are evaluated by integration of the FW-H equation on a porous surface encompassing the whole helicopter model. In order to highlight the BVI noise contribution, contour levels of the Overall Sound Pressure Level (OASPL) in the frequency range between the $6^{th}$ and the $40^{th}$ Blade Passage Frequency (BPF) are plotted. The improvement of the aerodynamic solution associated with the computational grid refinement, reflects directly into the improvement of the noise radiation prediction. Indeed, the noise footprint for the coarse mesh shows an overestimation of $2$ dB of the high-noise region in the advancing side and an underestimation of $4$ dB of the noise levels in the retreating side. Conversely, for the fine resolution case, the high-noise level lobe in the advancing side is correctly predicted, while the spot in the retreating side is underestimated by $2$ dB. From the above observations, it is possible to state that the fine mesh resolution provides a sufficient accuracy level and can be used in the reminder of this work to illustrate the effects of the blade deformation modeling and the effects of fuselage scattering.

### 3.2. Blade deformation effects

In this subsection, numerical results obtained with/without elastic blade deformation are compared in terms of unsteady air-loads, vertical tip-vortex positions and BVI noise footprint.

Figure 5 shows the effect of the blade elastic deformation modeling, as described in Section 2.2, on the $c_n M^2$ at $r/R = 0.87$. Taking into account the blade elastic deformation results in a more accurate prediction of the sectional air-loads along most of the rotor revolution, especially at locations where strong blade-vortex interactions occur and for the azimuthal sector between $90°$ and $270°$, where the elastic blade torsion is mainly responsible for the low-frequency load variation.

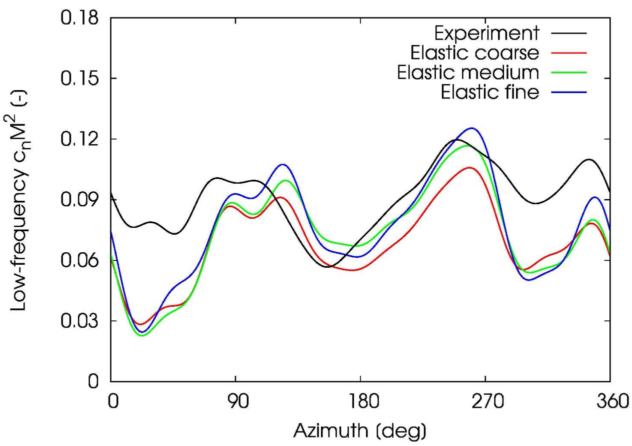


(a) *Low-frequency $c_n M^2$ content (up to $10$/rev)*

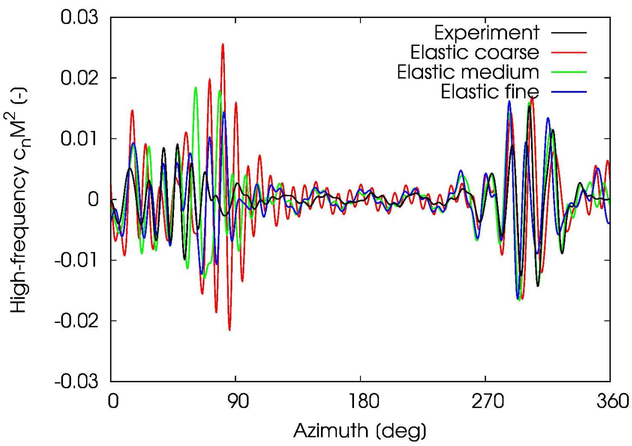


(b) *High-frequency $c_n M^2$ content (above $10$/rev)*

Figure 3: Frequency filtered $c_n M^2$ time histories at $r/R = 0.87$; mesh resolution effects.

To better stress the aforementioned aspects, it is useful to decompose the $c_n M^2$ coefficient into its low and high-frequency contents. The low-frequency contribution plotted in Fig. 6(a) confirms that the inclusion of the blade deformation improves the air-loads prediction, except for azimuthal position between $0°$ and $60°$, where the low-frequency contribution of the elastic rotor case is underestimated compared to the rigid rotor case. Moreover, as further highlighted in Fig. 6(b), taking into account the elastic blade deformation improves the accuracy of the high-frequency $c_n M^2$ contribution, and thus BVI phenomenon, in par-

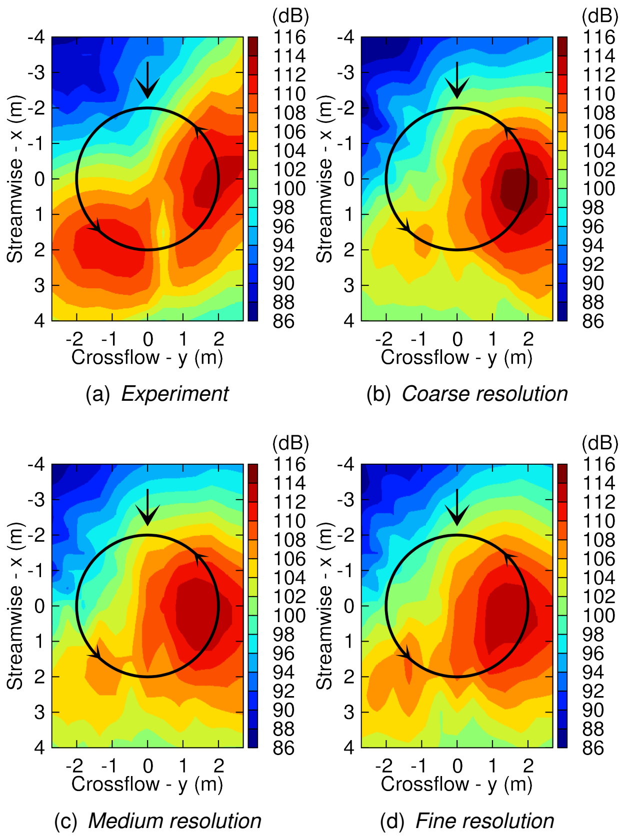


(a) *Experiment* (b) *Coarse resolution*

(c) *Medium resolution* (d) *Fine resolution*

Figure 4: Effect of mesh resolution on BVI noise footprint; OASPL contour levels from FW-H results ($6^{\text{th}}$ to $40^{\text{th}}$ BPF).

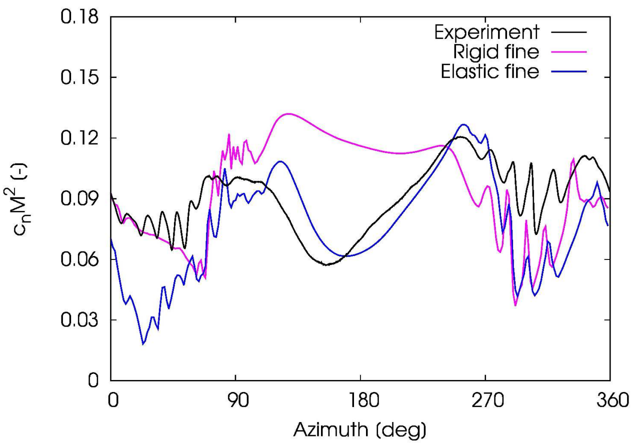


Figure 5: Time history of $c_n M^2$ at $r/R = 0.87$; blade deformation effects.

ticular in the retracting side.

Figures 7(a) and 7(b) show the tip-vortex position, in the hub reference frame, on two lateral planes placed in the advancing side (y-hub = $1.4$ m) and in the retreating side (y-hub = $-1.4$ m), respectively. In this work, the tip-vortex locations are determined by extracting the center of the vortex-core from vorticity

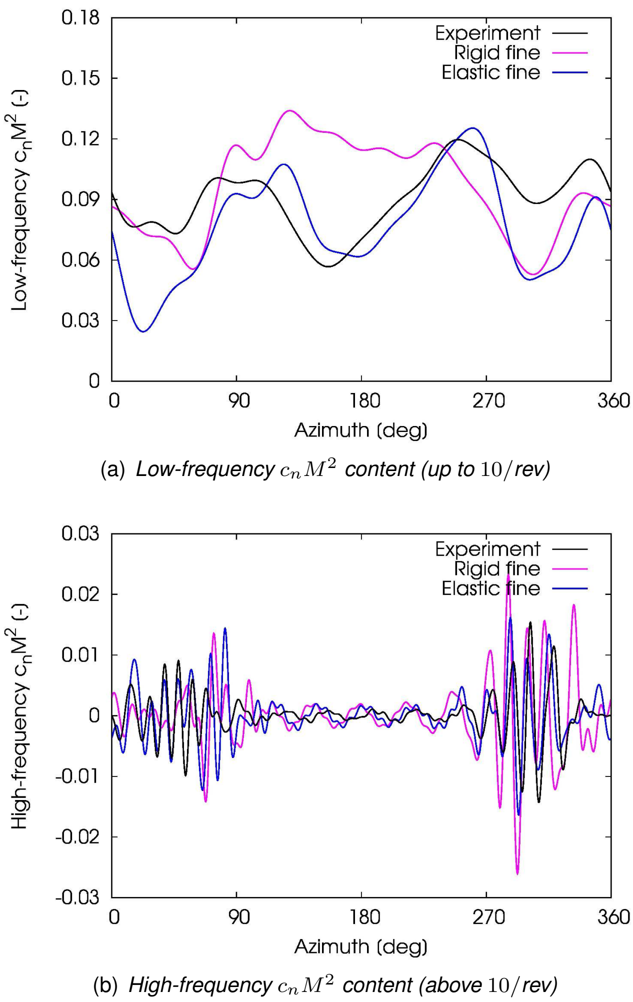


(a) *Low-frequency $c_n M^2$ content (up to $10$/rev)*

(b) *High-frequency $c_n M^2$ content (above $10$/rev)*

Figure 6: Frequency filtered $c_n M^2$ time histories at $r/R = 0.87$; blade deformation effects.

magnitude contour plots. Both in the advancing and retreating sides, the modeling of the blade elastic deformation results in a better agreement between numerical results and measurements. An accurate prediction of the vertical tip-vortex position represents a crucial aspect in BVI noise prediction, since, as mentioned before, the blade-vortex miss distance has a strong influence on the pressure fluctuations induced by the vortices on the blade. It is interesting to point out that, even if the elastic blade deformation is not directly simulated, modeling it has an equivalent dynamic effect on the flow and results in a more accurate development of the wake.

Finally, Figure 8 illustrates the effects of the blade elastic deformation on the predicted BVI noise footprint on a horizontal plane located $2.2$ m below the rotor hub. As already stressed, modeling the elastic deformation improves the accuracy of BVI noise prediction. Indeed, the elastic rotor setup is able to capture the high-noise lobe in the advancing side and the low-noise region in a very satisfactory way, even though

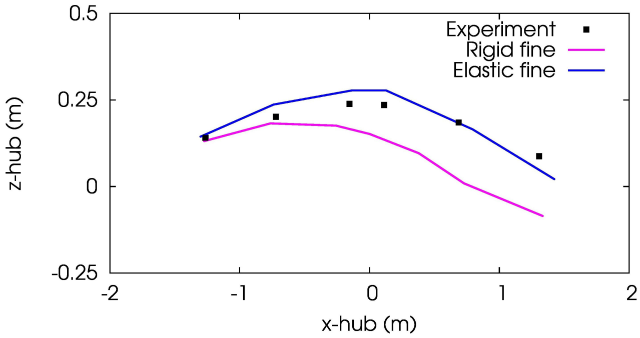


(a) *Advancing side, y-hub =* $1.4$ *m*

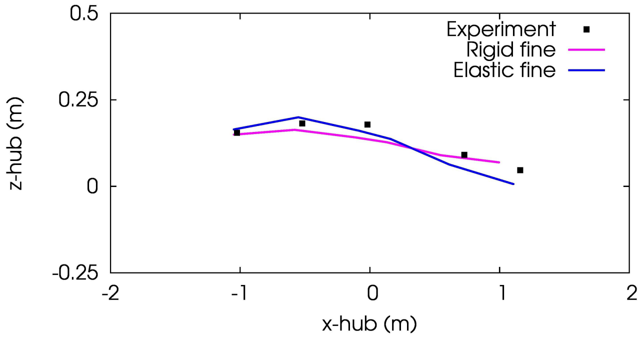


(b) *Retreating side, y-hub =* $-1.4$ *m*

Figure 7: Tip-vortex trace on vertical planes; blade deformation effects.

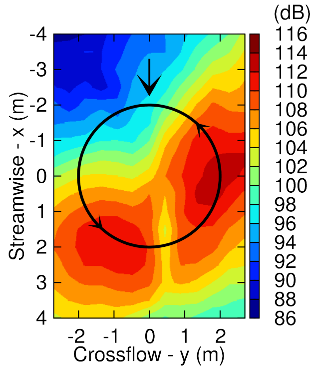


(a) *Experiment*

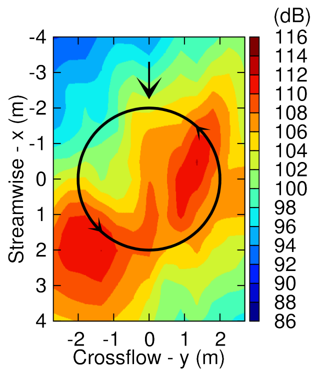


(b) *Rigid rotor*

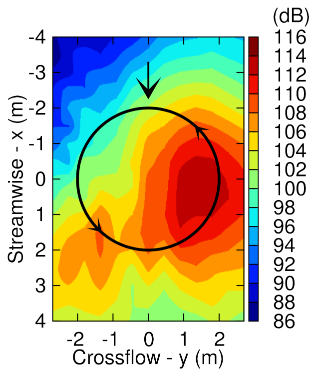


(c) *Elastic rotor,*

Figure 8: Effect of blade deformation on BVI noise footprint; OASPL contour levels from FW-H results ($6^{\text{th}}$ to $40^{\text{th}}$ BPF).

the high-noise lobe in the retreating side is underestimated by $2$ dB. Conversely, the rigid rotor results exhibit a better agreement with the measurements only in the retracting side, whereas the high-noise lobe in the advancing side is underestimated by $2$-$3$ dB, and the low-noise region in the top-left corner is not properly captured. It is worth mentioning that the present level of accuracy for the case of elastic rotor setup is higher than what obtained by using comprehensive codes, as reported in Refs.[8,9].

## 4. FUSELAGE SCATTERING STUDY

One of the possible causes of discrepancy between BVI noise measurements and isolated-rotor predictions, which is frequently mentioned in the literature, is the fuselage scattering. In this section, the fuselage scattering effects for the HART-II configuration are investigated numerically by performing two additional comparative simulations, one for an isolated rotor, and the other by replacing the HART-II wind-tunnel fuselage model with a more realistic geometry. Figure 9(a) shows the three configurations. The same mesh layout and resolution, computational setup, rotor geometry and operating conditions are used for the three cases. The HART-II fuselage is about $5$ m long and has the cross section length of about $0.8$ m, whereas for the realistic fuselage, the above dimensions are about $4.75$ m and $0.75$ m, respectively.

Since the presence of the fuselage affects the flow in proximity of the rotor, it is important to quantify this effect in terms of blade loading. Figure 10 shows the $c_n M^2$ coefficient time-history at $r/R = 0.87$ for the three cases. The main aerodynamic influence of the helicopter fuselage on the unsteady loads consists of an up-wash effect in front of the fuselage ($\Psi$ around $180°$) and a down-wash effect at the rear of the fuselage ($\Psi$ around $0°$). These are locations where no BVI occurs, therefore, the aerodynamic fuselage installation effects on the BVI noise can be neglected and any possible fuselage influence on the noise radiation is expected to have an acoustic origin.

Figure 11 shows the effect of fuselage on the BVI noise footprint on a carpet located $2.2$ m below the rotor hub. These results show that the presence of the fuselage does not affect significantly the noise radiation in the near-field, being the HART-II configuration slightly noisier, both in the advancing and retreating sides, compared to the other cases.

Figure 12 shows instantaneous snapshots of pressure time derivative on a carpet located $2.2$ m below the rotor hub. Here, the pressure time derivative, which is proportional to the dilatation field, is computed from the CFD pressure field. The acous-

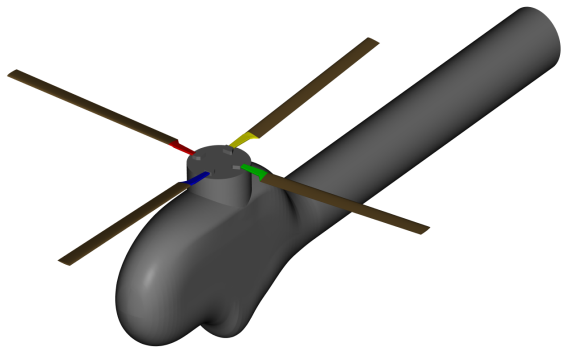

(a) *HART-II setup with wind-tunnel fuselage*

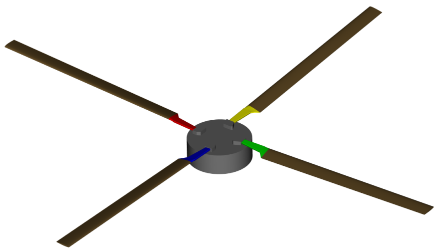

(b) *HART-II setup without fuselage*

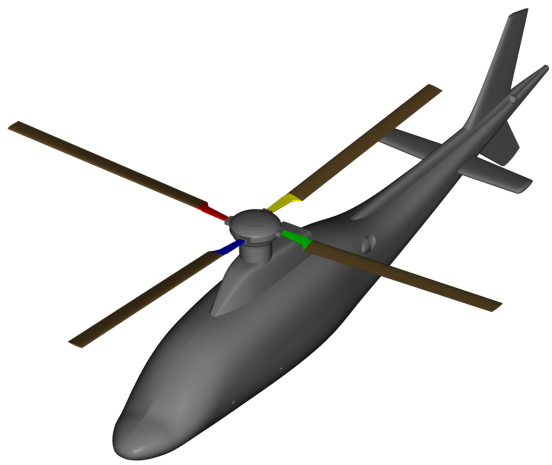

(c) *HART-II setup with realistic fuselage*

Figure 9: Illustration of the simulated helicopter configurations.

tic waves associated with BVI are clearly visible both in the advancing side and retreating side and reveal a near-field acoustic pattern which is qualitative quite similar for the three different configurations.

In order to better scrutinize the fuselage scattering effects, the noise footprint is evaluated on a carpet of $300 \times 300$ m located $15$ m below the helicopter. The noise levels are evaluated by using the FW-H formulation. One-third octave bands Sound Pressure Level (SPL) contours are computed for the bands reported in Table 2. The corresponding central-frequency acoustic wavelength is reported for the sake of comparison with the characteristic dimensions of the fuselage.

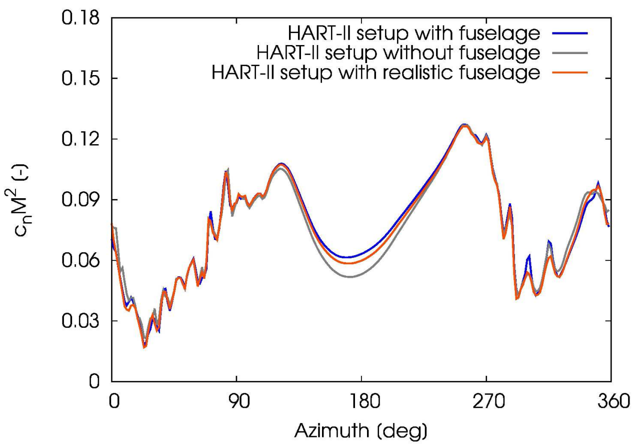


Figure 10: Time history of $c_n M^2$ at $r/R = 0.87$; fuselage effects analysis.

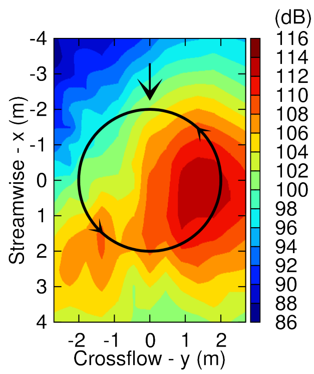


(a) *HART-II setup with fuselage*

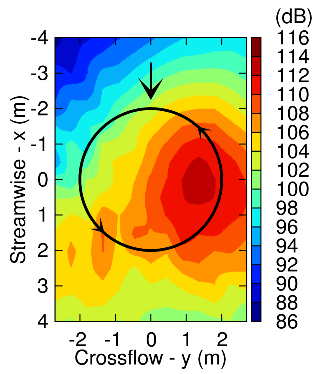


(b) *HART-II setup without fuselage*

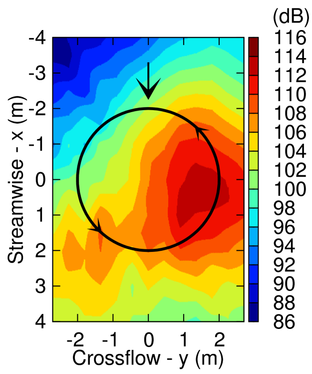


(c) *HART-II setup with realistic fuselage*

Figure 11: Effect of fuselage on BVI noise footprint; OASPL contour levels from FW-H results ($6^{\text{th}}$ to $40^{\text{th}}$ BPF).

lage.

Figure 13 shows the OASPL contour levels within the frequency range $416.81 \div 525.14$ Hz for the three helicopter configurations considered in this study. These results reveal that the presence of the fuselage (Figure 13(a) and Figure 13(c)) leads to an overall in-

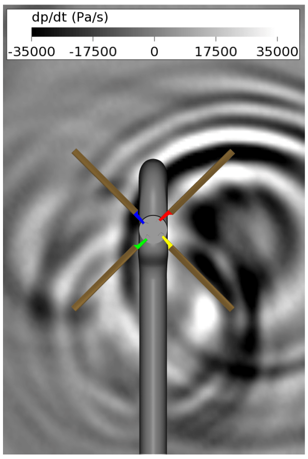


(a) *HART-II setup with fuselage*

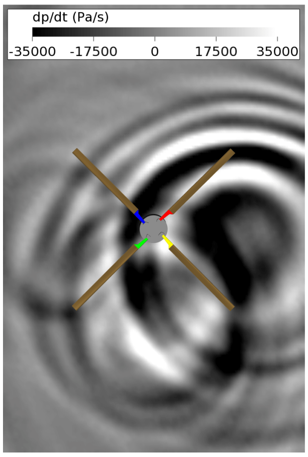


(b) *HART-II setup without fuselage*

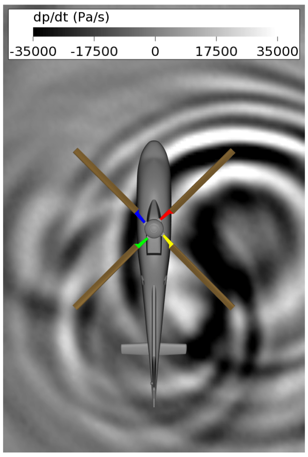


(c) *HART-II setup with realistic fuselage*

Figure 12: Pressure time derivative from CFD pressure field.

| $f_1\ (Hz)$ | $f_2\ (Hz)$ | $f_0\ (Hz)$ | $\lambda_0\ (m)$ |
|---|---|---|---|
| 416.81 | 525.14 | 467.85 | 0.73 |
| 525.14 | 661.64 | 589.46 | 0.58 |
| 661.64 | 833.62 | 742.67 | 0.46 |
| 833.62 | 1050.29 | 935.70 | 0.37 |
| 1050.29 | 1323.28 | 1178.91 | 0.29 |

Table 2: Frequency band limits, frequency band centers and corresponding acoustic wavelengths.

crement of the noise levels, especially on the sideline.

This overall noise increment due to fuselage scattering effects can be also observed for the other frequency bands. As a proof, Table 3 reports the extension of the ground area where the OASPL is higher than $65$ dB. The isolated rotor configuration is systematically quieter than the other installed rotor configurations.

To better discriminate how the presence of the fuse-

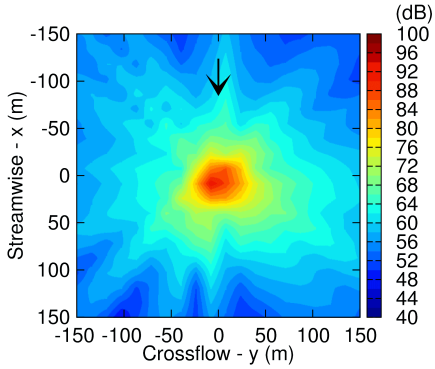


(a) *HART-II setup with fuselage*

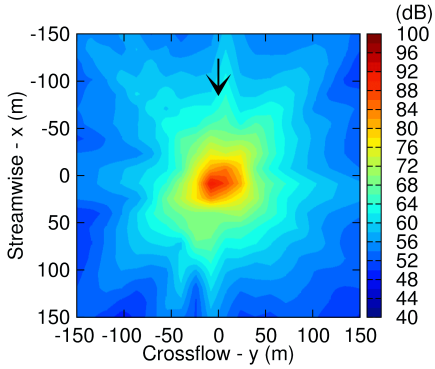


(b) *HART-II setup without fuselage*

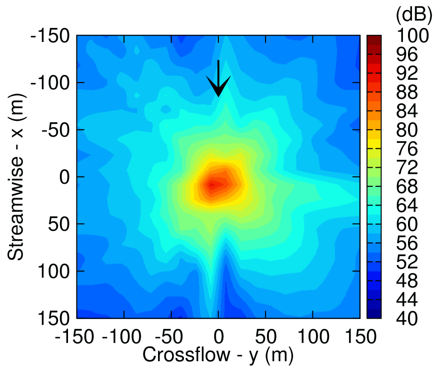


(c) *HART-II setup with realistic fuselage*

Figure 13: OASPL ($416.81 \div 525.14$ Hz) contour levels from FWH analogy; fuselage effects analysis.

| $f_1\ (Hz)$ | $f_2\ (Hz)$ | $Area > 65\ dB\ (m^2)$ | | |
|---|---|---|---|---|
| | | HII | IR | RF |
| 416.81 | 525.14 | 12825 | 11925 | 13950 |
| 525.14 | 661.64 | 17325 | 13500 | 15525 |
| 661.64 | 833.62 | 17100 | 14850 | 15975 |
| 833.62 | 1050.29 | 11700 | 11025 | 11250 |
| 1050.29 | 1323.28 | 10575 | 9675 | 9450 |

Table 3: Area of SPL over the threshold value of $65$ dB for different frequency bands: HART-II configuration (HII), Isolated Rotor (IR) and Realistic Fuselage (RF).

lage affects the noise field around the helicopter, Figures 14 to 18 show the $\Delta$SPL contour levels between the three different configurations. Specifically, HII-IR denotes $\Delta$SPL evaluated as the OASPL of the HART-II configuration minus the OASPL of the isolated rotor, whereas RF-IR corresponds to the OASPL of the realistic fuselage configuration minus the OASPL of the isolated rotor.

The HII-IR results show that the presence of the fuselage is responsible for a significant increment of the noise levels on the rear right-hand side of the helicopter in all the frequency bands considered. This is mainly due to the fact that strongest BVI takes place in the advancing side and thus on the right-hand side of the helicopter. A further increment of the noise levels can be also observed in the rear left-hand side of the helicopter, especially for the first three frequency bands. Moreover, some weak shielding effects, especially around the plane of symmetry and on the front part of the helicopter, are generated by the fuselage.

The RF-IR results show again that the main acoustic effect of the fuselage is the increment of the noise levels on the left, rear left and rear right-hand side of the helicopter for all the frequency bands considered. However, this effect seems to be less pronounced for the realistic fuselage configuration, especially as the frequency increases, and it is probably due to the quite different tail configurations between the HART-II and the realistic fuselage cases.

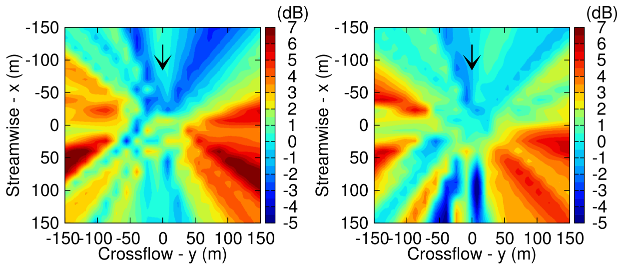


(a) *HII-IR* (b) *RF-IR*

Figure 14: $\Delta$SPL ($416.81 \div 525.14$ Hz) contour levels; fuselage effects analysis.

## 5. CONCLUSIONS

In this paper, the commercial CFD/CAA solver PowerFLOW® has been used to predict the unsteady aerodynamic loadings, the rotor wake and the noise radiation of the HART-II helicopter BVI benchmark configuration. A mesh resolution study was conducted and it revealed an acceptable level of mesh convergence, with reasonably good results in terms of noise footprint obtained using a resolution of $60$ voxels per blade chord (medium resolution) at a CPU cost of $1200$ hours per rotor revolution. Taking into account the blade elastic deformation through a combination of rigid blade pitching and blade plunging modeled as a wall velocity boundary condition led to very

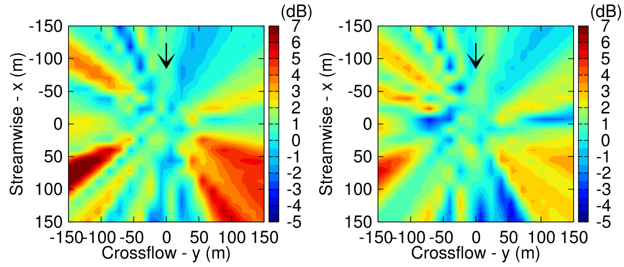


(a) *HII-IR* (b) *RF-IR*

Figure 15: $\Delta$SPL ($525.14 \div 661.64$ Hz) contour levels; fuselage effects analysis.

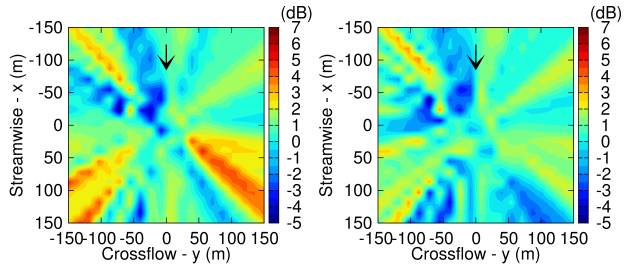


(a) *HII-IR* (b) *RF-IR*

Figure 16: $\Delta$SPL ($661.64 \div 833.62$ Hz) contour levels; fuselage effects analysis.

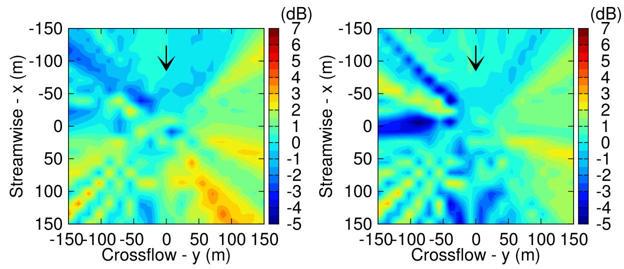


(a) *HII-IR* (b) *RF-IR*

Figure 17: $\Delta$SPL ($833.62 \div 1050.29$ Hz) contour levels; fuselage effects analysis.

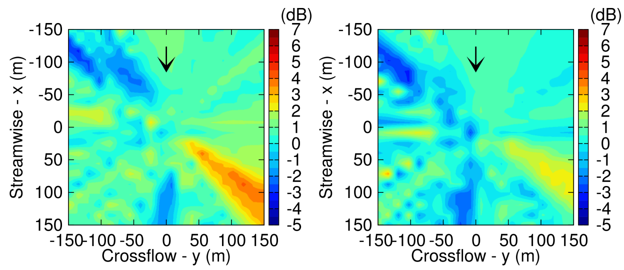


(a) *HII-IR* (b) *RF-IR*

Figure 18: $\Delta$SPL ($1050.29 \div 1323.28$ Hz) contour levels from FWH results; fuselage effects analysis.

promising aerodynamic and aeroacoustic results, with a substantial improvement in terms of sectional airloads, tip-vortex vertical position and noise radiation compared to a rigid rotor case. The current level of accuracy of the aeroacoustic results can be considered quite satisfactory if compared to the accuracy reported in the literature[8,9,36,37]. In the future, a further investigation of the blade torsion modeling will be carried out to improve the BVI loads in the advancing side and the noise footprint in the retracting side. Finally, the analysis on the fuselage effects has shown that, during a descent flight condition characterized by strong BVI, the fuselage aerodynamic influence on the noise sources is negligible, whereas the presence of the fuselage affects the noise directivity quite significantly, an effect which is more pronounced in the far-field sideline.

**ACKNOWLEDGEMENTS**

The authors gratefully acknowledge the provision of data that was used in this study by the members of the HART II team.



**REFERENCES**

[1] H. Y. Yung, "Rotor Blade–Vortex Interaction Noise," *Progress in Aerospace Sciences*, vol. 36, no. 2, pp. 97–115, 2000.

[2] Y. H. Yu, C. Tung, B. van der Wall, H.-J. Pausder, C. Burley, T. Brooks, P. Beaumier, Y. Delrieux, E. Mercker, and K. Pengel, "The HART-II test: Rotor Wakes and Aeroacoustics with Higher-Harmonic Pitch Control (hhc) Inputs-The Joint German/French/Dutch/Us Project," tech. rep., DTIC Document, 2002.

[3] B. G. van der Wall, B. Junker, C. Burley, T. Brooks, Y. Yu, C. Tung, M. Raffel, H. Richard, W. Wagner, E. Mercker, *et al.*, "The HART II Test in the LLF of the DNW-a Major Step Towards Rotor Wake Understanding," in *Proceedings of the 28th European Rotorcraft Forum, Bristol, England*, pp. 273–284, 2002.

[4] J. W. Lim, C. Tung, Y. H. Yu, C. L. Burley, T. Brooks, D. Boyd, B. Van Der Wall, O. Schneider, H. Richard, and M. Raffel, "HART-II: Prediction of Blade-Vortex Interaction Loading," tech. rep., DTIC Document, 2003.

[5] B. G. van der Wall, "2nd HHC Aeroacoustic Rotor Test (HART II)-Part I: Test Documentation," *Institute Report, IB-111-2003/31, ftp://HART-II@ ftp. dlr. de*, 2003.

[6] B. G. van der Wall and C. L. Burley, "2nd HHC Aeroacoustic Rotor Test (HART II)-Part II: Representative Results," *Institute Report, IB-111-2005/34, ftp://HART-II@ ftp. dlr. de*, 2005.

[7] "The Data Base of the HART II International Workshop." `https://rotorcraft.arc.nasa.gov/hart2/index.php`.

[8] B. G. van der Wall, J. W. Lim, M. J. Smith, S. N. Jung, J. Bailly, J. D. Baeder, and D. D. J. Boyd, "An Assessment of Comprehensive Code Prediction State-Of-The-Art Using the HART II International Workshop Data," *AHS International 68th Annual Forum*, 2012.

[9] B. G. van der Wall, J. W. Lim, M. J. Smith, S. N. Jung, J. Bailly, J. D. Baeder, and D. D. Boyd Jr, "The HART II International Workshop: an Assessment of the State-of-the-art in Comprehensive Code Prediction," *CEAS Aeronautical Journal*, vol. 4, no. 3, pp. 223–252, 2013.

[10] M. J. Smith, J. W. Lim, B. G. van der Wall, J. D. Baeder, R. T. Biedron, D. D. Boyd Jr, B. Jayaraman, S. N. Jung, and B.-Y. Min, "An Assessment of CFD/CSD Prediction State-of-the-art Using the HART II International Workshop Data," in *68th Annual Forum of the American Helicopter Society, Ft. Worth, TX*, 2012.

[11] M. J. Smith, J. W. Lim, B. G. van der Wall, J. D. Baeder, R. T. Biedron, D. D. Boyd Jr, B. Jayaraman, S. N. Jung, and B.-Y. Min, "The HART II International Workshop: an Assessment of the State of the art in CFD/CSD Prediction," *CEAS Aeronautical Journal*, vol. 4, no. 4, pp. 345–372, 2013.

[12] J. E. Ffowcs Williams and D. L. Hawkings, "Sound generated by turbulence and surfaces in arbitrary motion," *Philosophical Transactions of the Royal Society of London, Series A*, vol. A264, no. 1151, pp. 321–342, 1969.

[13] X. Nie, X. Shan, and H. Chen, "A lattice-boltzmann/finite-difference hybrid simulation of transonic flow," *AIAA Paper 2009-0139*, 2009.

[14] H. Chen, S. Chen, and W. Matthaeus, "Recovery of the navier-stokes equations using a lattice-gas boltzmann method," *Physical Review A*, vol. 45, no. 8, pp. 5339–5342, 1992.

[15] P. L. Bhatnagar, E. P. Gross, and M. Krook, "A model for collision processes in gases. i. small amplitude processes in charged and neutral one-component systems," *Physical Review*, vol. 94, no. 3, pp. 511–525, 1954.

[16] H. Chen, S. Kandasamy, S. A. Orszag, S. Succi, and V. Yakhot, "Extended boltzmann kinetic equation for turbulent flows," *Science*, vol. 301, no. 5633, pp. 633–636, 2003.

[17] V. Yakhot and S. A. Orszag, "Renormalization group analysis of turbulence. i. basic theory," *Journal of Scientific Computing*, vol. 1, no. 1, pp. 3–51, 1986.

[18] V. Yakhot, S. A. Orszag, S. Thangam, T. B. Gatski, and C. G. Speziale, "Development of turbulence models for shear flows by a double expansion technique," *Physics of Fluids A*, vol. 4, no. 7, pp. 1510–1520, 1992.

[19] C. M. Teixeira, "Incorporating turbulence models into the lattice-boltzmann method," *International Journal of Modern Physics C*, vol. 9, pp. 1159–1175, 1998.

[20] C. G. Alexander, H. Chen, S. Kandasamy, R. Shock, and S. R. Govindappa, "Simulations of engineering thermal turbulent flows using a lattice boltzmann based algorithm," *ASME-PUBLICATIONS-PVP*, vol. 424, pp. 115–126, 2001.

[21] A. Anagnost, A. Alajbegovic, H. Chen, H. Hill, C. Teixeira, and K. Molvig, "Digital physics analysis of the morel body in ground proximity," *SAE Paper 970139*, 1997.

[22] H. Chen, C. Teixeira, and K. Molvig, "Realization of fluid boundary conditions via discrete boltzmann dynamics," *International Journal of Modern Physics C*, vol. 9, no. 8, pp. 1281–1292, 1998.

[23] D. Casalino, A. F. P. Ribeiro, E. Fares, and S. Nölting, "Lattice-boltzmann aeroacoustic analysis of the lagoon landing gear configuration," *AIAA Journal*, vol. 52, no. 6, pp. 1232–1248, 2014.

[24] D. Casalino, A. F. P. Ribeiro, and E. Fares, "Facing rim cavities fluctuation modes," *Journal of Sound and Vibration*, vol. 333, no. 13, pp. 2812–2830, 2014.

[25] M. R. Khorrami, E. Fares, and D. Casalino, "Towards full aircraft airframe noise prediction: Lattice boltzmann simulations," *AIAA Paper 2014-2481*, June 2014.

[26] E. Fares, D. Casalino, and M. Khorrami, "Evaluation of airframe noise reduction concepts via simulations using a lattice boltzmann approach," *AIAA Paper 2015-2988*, 2015.

[27] D. Casalino, A. Hazir, and A. Mann, "Turbofan broadband noise prediction using the lattice boltzmann method," *AIAA Paper 2016-2945*, 2016.

[28] E. Envia, "Fan noise source diagnostic test-vane unsteady pressure results," *AIAA Paper 2002-2430*, 2002.

[29] D. Casalino, "An advanced time approach for acoustic analogy predictions," *Journal of Sound and Vibration*, vol. 261, no. 4, pp. 583–612, 2003.

[30] F. Farassat and G. P. Succi, "The prediction of helicopter discrete frequency noise," *Vertica*, vol. 7, no. 4, pp. 309–320, 1983.

[31] P. Di Francescantonio, "A new boundary integral formulation for the prediction of sound radiation," *Journal of Sound and Vibration*, vol. 202, no. 4, pp. 491–509, 1997.

[32] O. Schneider and B. G. van der Wall, "Preparation of SPR Data from HART II," *Institute Report, IB-111-2003/07, ftp://HART-II@ ftp. dlr. de*, 2003.

[33] O. Schneider and B. G. van der Wall, "Preparation of SPR Data from HART II-Final Analyzing Methods and Results," *Institute Report, IB-111-2003/20, ftp://HART-II@ ftp. dlr. de*, 2003.

[34] O. Schneider and B. G. van der Wall, "Completion of SPR Data Analysis from HART II," *Institute Report, IB-111-2004/07, ftp://HART-II@ ftp. dlr. de*, 2007.

[35] B. G. van der Wall, "Mode Identification and Data Synthesis of HART II Blade Deflection Data," *Institute Report, IB-111-2007/28, ftp://HART-II@ ftp. dlr. de*, 2007.

[36] G. Gopalan, J. Sitaraman, J. D. Baeder, and F. H. Schmitz, "Aerodynamic and Aeroacoustic Prediction Methodologies with Application to the HART II Model Rotor," *AHS International 62nd Annual Forum, Phoenix, AZ*, 2006.

[37] D. D. Boyd Jr, "HART-II Acoustic Predictions Using a Coupled CFD/CSD Method," *AHS International 65th Annual Forum, Ft. Worth, TX*, 2009.